

Submitted April 12, 2005 ; Accepted May 6, 2005 (to PASP)

Thermal evolution and activity of Comet 9P/Tempel 1 and simulation of a deep impact

Gal Sarid and Dina Prialnik,¹
Karen J. Meech and Jana Pittichová,²
and
Tony L. Farnham³

ABSTRACT

We use a quasi 3-D thermal evolution model for a spherical comet nucleus, which takes into account the diurnal and latitudinal variation of the solar flux, but neglects lateral heat conduction. We model the thermal evolution and activity of Comet 9P/Tempel 1, in anticipation of the *Deep Impact* mission encounter with the comet. We also investigate the possible outcome of a projectile impact, assuming that all the energy is absorbed as thermal energy. An interesting result of this investigation, is that the estimated amount of dust ejected due to the impact is equivalent to 2–2.6 days of activity, during "quiet" conditions, at perihelion.

We show that production rates of volatiles that are released in the interior of the nucleus depend strongly on the porous structure, in particular on the surface to volume ratio of the pores. We develop a more accurate model for calculating this parameter, based on a distribution of pore sizes, rather than a single, average pore size.

Subject headings: comets: general — Comet 9P/Tempel 1

¹Department of Geophysics and Planetary Sciences, Sackler Faculty of Exact Sciences, Tel Aviv University, Ramat Aviv 69978, Israel

²Institute for Astronomy, 2680 Woodlawn Drive, Honolulu, HI 96822

³Department of Astronomy, University of Maryland, College Park, MD 20742-2421

1. Introduction

Comet 9P/Tempel 1 is the target of NASA's *Deep Impact* mission (Belton and A'Hearn 1999, Meech et al. 2000, A'Hearn et al. 2005). The spacecraft, successfully launched on January 12, 2005, and due to encounter the comet on UT 5:52 (± 3 min) July 4, 2005, will collect images of the nucleus, and release a smaller projectile spacecraft. The projectile will maneuver its path for a collision with the nucleus of the target comet.

Comet 9P/Tempel 1 was first discovered in 1867, and recovered in 1873 and 1879. In 1881, the comet passed close to Jupiter, its orbit changed and it was lost. Later investigations (Marsden 1963) revealed that it had undergone two more close encounters with Jupiter, in 1941 and 1957. The comet reappeared in 1967 and since that time it has been observed at every apparition. Its present orbital period is 5.5 years and the perihelion distance is 1.506 AU.

In anticipation of the mission, comet 9P/Tempel 1 has been intensively observed by both professional and amateur astronomers (Lamy et al. 2001, Meech 2002) and data about its size, rotation, production rates, etc., has accumulated (Fernández et al. 2003, Belton et al. 2005). On the theoretical side, models have been developed to simulate the impact and its consequences (Schultz and Anderson 2005, Wünnemann et al. 2005). It is impossible, however, to simulate the impact accurately, since very little is known about the properties of cometary material. Clearly, the impact energy — originally kinetic — will divide between mechanical and thermal energies, but the proportion will be strongly determined by the nature of cometary material: its strength, porosity, thermal conductivity, and so forth.

Since the dynamical side of the impact has already been investigated in detail (Nolan et al. 1996, Housen 2002, Schultz et al. 2002), we focus in this paper on the thermal aspect. We first choose an initial model that matches as well as possible the observations of comet 9P/Tempel 1. This is achieved by running a number of models, for different assumptions and parameter combinations, through several orbital revolutions. The composition of these models will be assumed to include water ice, dust and 5 additional volatile species. A "thermal" impact on this model will then be simulated.

The evolution — both long-term, prior and following the impact, and short-term during the event itself — will be calculated by means of a quasi-3D code (Prialnik et al. 2005). This code takes into account diurnal and latitudinal variations, but neglects lateral heat conduction, and is an expanded version of the code used by Cohen et al. (2003).

In Section 2 we briefly describe the numerical code. Section 3 describes improvements implemented to the code that take into account a pore size distribution, rather than an average (fixed) pore size. Next, in Section 4 we describe ground-based observations that have

been recently carried out in anticipation of the *Deep Impact* mission in order to determine the comet's activity levels as a function of heliocentric distance. We include a subset of the observations in this paper for the purpose of modeling the dust coma so that we can obtain dust fluxes and the heliocentric distances between which the comet is active as constraints and tests for the thermal models. In the following Section 5 we show the results of numerical calculations for the thermal evolution of comet 9P/Tempel 1 along several orbital revolutions. The simulation of the impact and its consequences are described and discussed in Section 6. Our main conclusions may be found in Section 7.

2. Numerical model and parameters

Our model assumes a porous, spherical and initially homogeneous nucleus composed of amorphous and crystalline water ice, dust, and 5 other volatile species: CO, CO₂, HCN, NH₃, and C₂H₂. The equations of energy and mass conservation for this system are briefly summarized below (using standard notation, e.g., Prialnik et al. 2005).

We use a quasi-3D approach, where diurnal and latitudinal temperature variations are calculated as they result from uneven surface heating by solar radiation onto a spinning comet. Lateral heat conduction is neglected, and so heat is assumed to flow radially (perpendicular to the surface). Thus, different points on the surface do not interact. This simple approach is justified by the low thermal conductivity of cometary ice mixtures and by the thinness of the skin-depth (see Cohen et al. 2003).

The bulk mass density ρ and porosity Ψ are given, respectively, by

$$\rho = \rho_a + \rho_c + \rho_v + \sum_{\alpha} (\rho_{s,\alpha} + \rho_{g,\alpha}) + \rho_d, \quad (1)$$

$$\Psi = 1 - (\rho_a + \rho_c)/\varrho_{\text{ice}} - \sum_{\alpha} \rho_{s,\alpha}/\varrho_{\alpha} - \rho_d/\varrho_d, \quad (2)$$

where ϱ is the specific density of a species α . The meaning of indices is: a - amorphous water ice, c - crystalline water ice, ice - when the phases are indistinguishable, v - water vapor, s and g - solid and gaseous phases of a volatile species, respectively, and d - dust. The partial pressure, assuming an ideal gas, is

$$P_{\alpha} = \frac{\mathcal{R}_g \rho_{g,\alpha} T}{\Psi \mu}. \quad (3)$$

Because amorphous ice has a tendency to convert to the crystalline form spontaneously, we have

$$\frac{\partial \rho_a}{\partial t} = -\lambda \rho_a, \quad (4)$$

where λ is the rate of crystallization. If f is the total fraction of occluded gas, $\sum_\alpha f_\alpha = f$, the equations of mass conservation are

$$\frac{\partial \rho_c}{\partial t} = (1 - f)\lambda \rho_a - q_v, \quad (5)$$

$$\frac{\partial \rho_v}{\partial t} + \nabla \cdot \mathbf{J}_v = q_v, \quad (6)$$

for H_2O in both phases, and similarly,

$$\frac{\partial \rho_{g,\alpha}}{\partial t} + \nabla \cdot \mathbf{J}_\alpha = f_\alpha \lambda \rho_a + q_\alpha, \quad \frac{\partial \rho_{s,\alpha}}{\partial t} = -q_\alpha, \quad (7)$$

for the other volatile species. Taking into account energy conservation throughout the nucleus, and combining with the mass conservation equations, we obtain the heat diffusion equation in the form

$$\sum_\alpha \rho_\alpha \frac{\partial u_\alpha}{\partial t} - \nabla \cdot (K \nabla T) + \left(\sum_\alpha c_\alpha \mathbf{J}_\alpha \right) \cdot \nabla T = \lambda \rho_a \mathcal{H}_{\text{ac}} - \sum_\alpha q_\alpha \mathcal{H}_\alpha, \quad (8)$$

where \mathcal{H}_{ac} is the heat released upon crystallization, and \mathcal{H}_α is the heat of sublimation. The above set of time-dependent equations is subject to constitutive relations: $u(T)$, $\lambda(T)$, $q_\alpha(T, \Psi, r_p)$, $\mathbf{J}_\alpha(T, \Psi, r_p)$, $K(T, \Psi, r_p)$, where r_p denotes pore radius. These relations require additional assumptions for modeling the structure of the nucleus.

Measurements by Schmitt et al. (1989) have shown that the rate of crystallization is given by

$$\lambda(T) = 1.05 \times 10^{13} e^{-5370/T} \text{ s}^{-1}. \quad (9)$$

The rate of sublimation — mass per unit volume of cometary material per unit time — is given by

$$q_\alpha = S(\Psi, r_p) \left[(P_{\text{vap},\alpha}(T) - P_\alpha) \sqrt{\frac{\mu_\alpha}{2\pi R_g T}} \right], \quad (10)$$

where the term in square brackets represents the sublimation rate per unit surface area, and S represents the surface to volume ratio, which is a function of the given porosity and pore radius. The saturated vapor pressure, P_{vap} , is given by the Clausius - Clapeyron equation:

$$P_{\text{vap}} = P_0 \exp^{-B/T}, \quad (11)$$

where $P_0 = 3.56 \times 10^{12} \text{ N m}^{-2}$, and $B = 6141.667 \text{ K}$ (Fanale and Salvail 1984).

Dust is assumed to be, in part, dragged along with the gas flowing through pores and, in part, lifted off the nucleus surface by the sublimating vapor. For the former, the dust

velocity is assumed to be equal to the gas velocity (see Podolak and Prialnik 1996). An efficiency factor is calculated, to take account of a dust size distribution that allows only grains up to a critical size to be dragged or lifted off. The rest may accumulate to form a dust mantle. The efficiency factor may be adjusted so as to allow or prevent the formation of a sealing mantle (see also Prialnik et al. 2005 and references therein).

The equations of mass conservation and energy transport are second-order in space and hence each require two boundary conditions. One boundary condition for eq.(8) is vanishing heat flux at the center. The second one is obtained from the requirement of energy balance at the surface:

$$F(R) = \epsilon\sigma T(R, t)^4 + \mathcal{F}P_{\text{vap}}(T) \sqrt{\frac{\mu}{2\pi R_g T}} \mathcal{H} - (1 - \mathcal{A}) \frac{L_{\odot}}{4\pi d_H(t)^2} \cos z. \quad (12)$$

In the simple case considered here, of a rotational axis that is perpendicular to the orbital plane, the solar zenith angle is given in terms of latitude θ , and hour angle $\varphi = (2\pi/P_{\text{rot}})t$,

$$\cos z = \cos\theta \cos\varphi. \quad (13)$$

The factor $\mathcal{F} \leq 1$ represents the fractional area of exposed ice, since the surface material is a mixture of ice and dust, and can be written as

$$\mathcal{F} = \left(1 + \frac{\varrho_{\text{ice}} \rho_d}{\varrho_{\text{ice}} \varrho_d} \right)^{-1} \quad (14)$$

(Crifo and Rodionov 1997).

Similarly to the heat flux, the mass (gas) fluxes vanish at the center. At the surface, R , the gas pressures are those exerted by the coma; in the lowest approximation they may be assumed to vanish: $P_{\alpha}(R, t) = 0$. It should be mentioned that the simple (and commonly used) outer boundary conditions for both energy and gas fluxes have been recently examined in more detail by Davidsson and Skorov (2002, 2004). Back-scattering of molecules leaving the nucleus surface and penetration of solar radiation into a thin sub-surface layer of the nucleus have been shown to affect the surface and sub-surface temperatures. These temperatures, however, are equally affected by the other approximations of the model (such as sphericity or homogeneity of surface structure), not to mention the uncertainty in the thermal conduction coefficients. Nevertheless, production rates are far *less* affected by these factors. For example, if back scattering reduces the net amount of sublimation at a given temperature, the surface temperature increases, but with it the sublimation rate increases as well. In fact, at low heliocentric distances, the amount of sublimation may be quite accurately calculated simply by $(1 - \mathcal{A})L_{\odot} \cos z / (4\pi d_H^2 \mathcal{H})$, *independently* of the surface temperature.

Table 1: Orbital elements and nucleus characteristics

Parameter	Symbol	Value	Units
Semi-major axis	a	3.12	AU
Eccentricity	e	0.517491	
Effective radius	R	3.3	km
Geometric albedo	\mathcal{A}	0.04	
Nucleus spin period	P_{rot}	41.85	hr
Dust mass fraction	X_{d}	0.5	
Ice mass fraction	X_{ice}	0.5	
Porosity	Ψ	0.5	
Dust density	ϱ_{d}	3250	kg m^{-3}
H_2O ice density	ϱ_{ice}	917	kg m^{-3}
Dust heat capacity	c_{d}	1.3×10^3	$\text{J kg}^{-1} \text{ K}^{-1}$
Ice heat capacity	c_{ice}	$7.49T + 90$	$\text{J kg}^{-1} \text{ K}^{-1}$
Dust conductivity	K_{d}	10	$\text{J m}^{-1} \text{ s}^{-1} \text{ K}^{-1}$
C-Ice conductivity	K_{c}	$5.67 \times 10^2/T$	$\text{J m}^{-1} \text{ s}^{-1} \text{ K}^{-1}$
A-Ice diffusivity	$K_{\text{a}}/(c_{\text{ice}}\varrho_{\text{ice}})$	3×10^{-7}	$\text{m}^2 \text{ s}^{-1}$

The numerical code solves the heat diffusion and mass conservation equations using a fully implicit difference scheme (see Prialnik 1992). In order to obtain a better resolution near the surface, where the temperature gradient is steepest, the layers are progressively thinner towards the surface. With the spin vector perpendicular to the orbital plane, results for 6 hour angles are recorded: $\varphi = 0/360^\circ, 60^\circ, 120^\circ, 180^\circ, 240^\circ, 300^\circ$, a different one at each time-step. Separate calculations are carried out for latitudes corresponding to $\cos \theta = 1, 0.75, 0.5, 0.25$, that is, between the equator ($\theta = 0^\circ$) and a near-pole angle ($\theta = 75.5^\circ$). The physical parameter values used in the model calculations are given in Table 1.

3. Properties of a porous nucleus structure

A cold, icy porous medium allows for sublimation from the pore walls and condensation onto them, as well as for flow of — usually dilute — gas through the pores. The three fundamental properties that affect these processes are the porosity Ψ , the surface to volume ratio (SVR) S and the permeability ϕ . The first is defined as the total volume of pores per given bulk volume, and the second, as the total interstitial surface area of the pores per given bulk volume. The permeability is, up to a numerical constant, the proportionality coefficient

between the mass flux and the gradient of P/\sqrt{T} that drives the flow of mass, where P and T are the gas pressure and temperature, respectively.

In order to determine these three properties, a model of the porous structure is required. A commonly used one in modeling cometary interiors is that of a bundle of unconnected cylindrical tortuous capillary tubes (Mekler et al. 1990), where the tortuosity ξ , defined as the ratio of capillary length to linear distance, is taken as a free parameter. Another free parameter is the pore (capillary) radius r , for which some reasonable average pore size is assumed. These assumptions result in very simple expressions for S and ϕ in terms of Ψ , ξ and r :

$$S = \frac{2\Psi}{r}, \quad \phi = \frac{\Psi r}{\xi^2}. \quad (15)$$

These expressions imply, however, that *all* capillaries are of the *same* radius. If r represents the mean of a distribution of pore sizes, the simple formulae above cease to be correct, a fact that has been largely overlooked in previous calculations. There is, however, a price to pay for a more realistic approach to pore sizes, and it involves a larger number of parameters for defining the medium. Nevertheless, we shall show that the deviations from eqs.(15) may be quite considerable and thus worth the price.

Starting from the same model of cylindrical tortuous capillaries, we assume the radii to vary according to some size distribution, and consider a volume of unit thickness. Let $N(r)dr$ be the number of capillaries with radii between r and $r + dr$ crossing a unit area. Keeping in mind that for a capillary tube, $\phi \propto r^3/\xi$ (Gombosi 1994), the three fundamental properties of a porous medium are, in fact, moments of the distribution function:

$$S = \xi \int 2\pi r N(r) dr \quad (16)$$

$$\Psi = \xi \int \pi r^2 N(r) dr \quad (17)$$

$$\phi = \frac{\pi}{\xi} \int r^3 N(r) dr \quad (18)$$

(cf. Prialnik et al. 2005). It follows that

$$\phi = \frac{\Psi \int r^3 N(r) dr}{\xi^2 \int r^2 N(r) dr} = \frac{\Psi}{\xi^2} \bar{r} \quad (19)$$

while

$$S = 2\Psi \frac{\int r N(r) dr}{\int r^2 N(r) dr} = 2\Psi \left(\frac{\bar{r}}{r} \right), \quad (20)$$

where \bar{r} in eq.(19) is the mean pore radius weighted by the volume fraction occupied by capillaries of radii in the range $(r, r + dr)$. We note that eqs.(19) and (20) are similar to

(15), except that S depends on the harmonic mean of $(\frac{1}{r})$, rather than on the inverse of the mean. If we adopt \bar{r} as the free parameter, then the expression for S in eq.(15) should be corrected by a factor

$$C = \bar{r} \left(\frac{1}{r} \right) = \frac{\int r^3 N(r) dr \int r N(r) dr}{\left(\int r^2 N(r) dr \right)^2}. \quad (21)$$

A reasonable distribution function for pore size is a power law, since grains ejected from comet nuclei have a power law size distribution (see below), and comets are believed to be formed by uncompacted aggregations of grains, in which case the grain and pore size distributions should be similar. Thus, we assume

$$N(r) \propto r^{-\alpha} \quad \text{for} \quad r_{\min} < r < r_{\max}, \quad (22)$$

which depends on 4 parameters: the normalization factor, the exponent α and the range of the distribution defined by r_{\min} and r_{\max} . Instead, besides α , we may choose to assume values for the porosity Ψ (serving as a normalization factor), the average pore radius \bar{r} (in order to be able to compare results with the former, simpler approach), and the ratio

$$X \equiv r_{\min}/r_{\max} < 1. \quad (23)$$

The resulting correction factor for the SVR,

$$C_X(\alpha) = \frac{(3 - \alpha)^2}{(4 - \alpha)(2 - \alpha)} \frac{(1 - X^{4-\alpha})(1 - X^{2-\alpha})}{(1 - X^{3-\alpha})^2} \quad (24)$$

is plotted in Fig.1 for several values of X . Following the distribution of dust grains inferred from observations, typical parameter values are $X = 10^{-3} - 10^{-4}$ and $3 \leq \alpha \leq 4$ (Fulle et al. 1997, Jockers 1999, Harker et al. 2002).

We note, therefore, that for given porosity and average pore size, taking into account a pore size *distribution* can increase the SVR by up to a factor of 100. Moreover, large corrections correspond precisely to that narrow range of α values deduced from observations. The effect of a large SVR should manifest itself both externally, through the production rates of volatiles, and internally, through composition profiles. Both are bound to affect, for example, the interpretation of the upcoming *Deep Impact* observations. A comparison of model results obtained with and without the correction factor for the SVR will be shown in Section 5.

4. New Ground-Based Observations

In order to prepare for the *Deep Impact* encounter, the *Deep Impact* team has undertaken a large observing campaign to characterize the nucleus and the levels of activity (Meech et al.

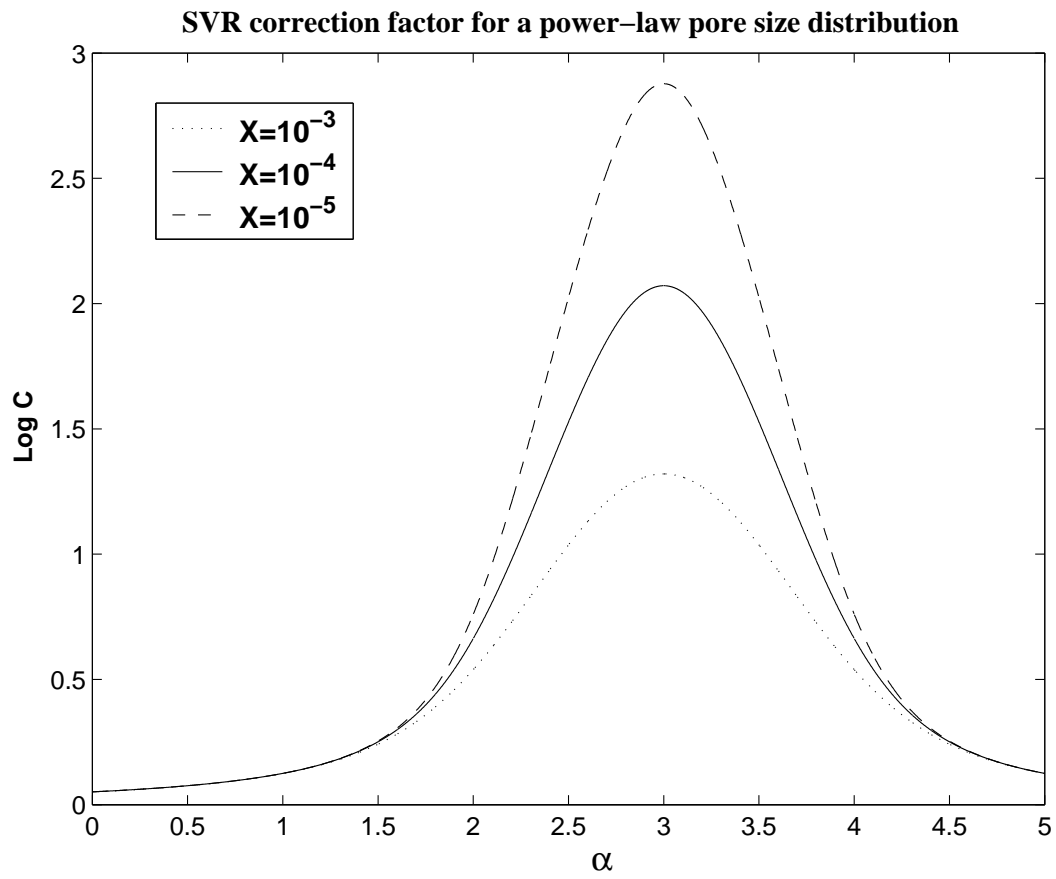


Fig. 1.— The correction factor of the SVR parameter, as a function of the power law exponent, for different ratios of minimal to maximal pore size. Note that the interval commonly used for pore size distribution ($3 < \alpha < 4$) gives a factor ≥ 10 .

2005). From past apparitions it was known that this comet typically exhibits a sharp rise in brightness near 200 days pre-perihelion (Meech et al. 2005). Optical CCD images have been obtained regularly since 1997 to monitor the development of activity and the cessation of activity as the comet moved to aphelion in early 2002. This comet is well placed for observing every other apparition, and the early 2000 perihelion passage was only moderately good for dust dynamical modeling, but was our first chance to measure the dust parameters for this comet. Nevertheless, we have a large data set accumulated for this purpose beginning in January and March 1999 pre-perihelion, and continuing from August 2000 through January 2001.

Finson-Probstein (1968) dust-dynamical models use the observed extent and morphology of the dust coma to determine the relative velocity distribution, size distribution and production rates of the dust leaving the nucleus as a function of heliocentric distance. These models evaluate the motion of a suite of particles after leaving the nucleus under the influence of solar radiation pressure and gravity. The scattered light from the dust is added together and fit to the surface brightness of the observed coma.

In order to use dust imaging to constrain the velocity and size distributions as well as the production rates, the images must be taken at the appropriate times:

- Small particles move rapidly away from the nucleus (and out of the field of view), so in order to constrain the size distribution from models, many images closely spaced in time need to be obtained.
- Large grains, which move slowly along the orbit, need observations equally spaced over time periods of months for proper modeling.
- Small particles tend to lie in the anti-solar direction, whereas large particles lag behind in orbit.
- The predicted dust trajectories (syn-curves, comprising the locus of the synchrones and syndynes) should be spread out in the plane of the sky so that good constraints can be obtained for the model parameters.
- Very circular orbits tend to have widely spaced syn-curves, but changes with time are harder to see. Comets on very elliptical orbits have problems inbound when the large particles fall along the sun-to-comet radius vector (and overlap the syn-curves for the small grains). 9P/Tempel 1 is a good comet for modeling in that its orbit has an intermediate eccentricity.

For comet 9P/Tempel 1, the syn-curves were predicted to be moderately good for the fall of 2000 observations (post-perihelion), and excellent starting in February 2005 through the encounter. We will report on the preliminary modeling for the observations obtained during fall 2000.

Kron-Cousins R-band images were obtained on 2000 Aug 21 and 2000 Sep 30, using the University of Hawaii 2.2m telescope on Mauna Kea and the the Tektronics 2048×2048 CCD (read noise = 7e^- , gain = $1.4\text{e}^-/\text{ADU}$, plate scale = $0.219''/\text{pixel}^{-1}$). Flat fields were obtained on the twilight sky, and standard reduction procedures were able to flatten the data to with 0.4% across the CCD. The nights were photometric, and standard stars from Landolt (1992) were observed on each night.

Composite images were made by using measurements of the centroids of a large number of field stars and the centroids were used to compute the offsets between the individual images (from telescope guiding errors). After the offsets were applied, the ephemeris rates for 9P/Tempel 1 were used, in combination with the image plate scale, to calculate shifts to simulate guiding at non-sidereal rates, and then the images were added. Selected field stars, close to the comet, were fit and removed from composite image. The resultant images are shown in Figure xx (attached to the paper).

Fig.xx.– Composite images of comet 9P/Tempel 1 (left) from 2000 Aug. 21 ($r=2.54$ AU), composed of 26×300 sec R images and (right) from 2000 Sep. 30 ($r=2.77$ AU) composed of 42×300 sec R images. Images are $180 \times 180''$, with N at the top and E to the left.

Using a code developed by Farnham (1996), Finson-Probstein dust dynamical models were fit to the images, and preliminary results are shown in Table 2. Contour fits to the images are shown in Figure 2.

Table 2: Finson-Probstein Model Fit

Parameter	Value
Smallest particles	$3 \mu\text{m}$
Largest particles	3 mm
Emission start	<i>perihelion</i> – 100 days
Maximum dust output	<i>perihelion</i> – 60 days
Emission decline	<i>perihelion</i> + 260 days
Velocity ($v(\beta)$) ^[1]	$v(r_{\min})/v(r_{\max}) \approx 40$
$\alpha^{[2]}$	3.1

Notes: ^[1] $\beta = F_{\text{rad}}/F_{\text{grav}} = 5.74 \times 10^{-4} Q_{\text{rp}}/\varrho_d r$, is a proxy for grain size, where Q is the radiation pressure scattering efficiency. ^[2] Fit value for the slope of the particle size distribution.

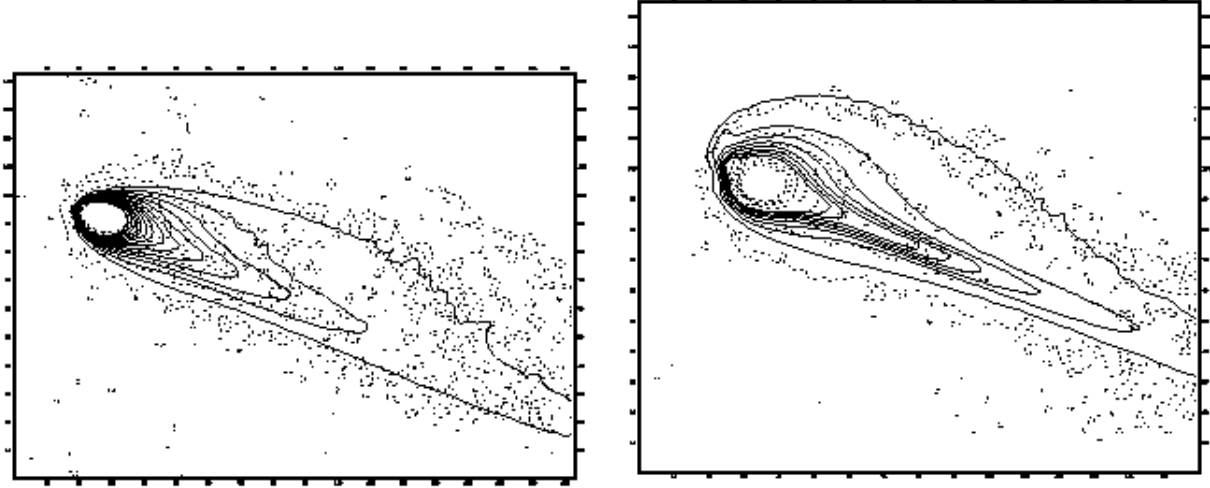


Fig. 2.— Finson-Probstein dust dynamical model fits to the data on Aug. 21 (left) and Sep. 30 (right), 2000 plotted on contours from the composite images.

5. Results of evolutionary calculations

Since little is known about any comet's structure and composition, our first task was to choose the structural and compositional parameters. The composition was chosen by running several models of various generic composition, but identical structure — as listed in Table 3 — and comparing the resulting production rates to available observations (Cochran et al. 1992, Osip et al. 1992). This is shown in Fig.3. The model for which agreement was obtained for all observed species available was then chosen as the *working model*. The dust production rate of this model, shown in Fig.4 agrees very well with the results derived from ground-based observations described in Section 4. We note, in particular, the times of rise, maximum and decline in the rate of dust emission, compared to those of Table 2. The magnitude corresponding to the dust production rate at maximum is about 9; varying the average grain size and/or dust grain density may result in a change of ± 0.5 mag (for a correlation between dust production and magnitude, and perihelion magnitudes, see Meech et al. 2005, 2002).

Guided by the dust grain size distribution derived from observations, we adopted for the pore size distribution inside the nucleus a slightly steeper power law, with $\alpha = 3.5$, an average pore size of $100 \mu\text{m}$, and a ratio $X = 10^{-4}$. According to the discussion in Section 3, $\bar{r} \approx \sqrt{r_{\min} r_{\max}}$, which results in a size range between $r_{\min} = 1 \mu\text{m}$ and $r_{\max} = 1 \text{ cm}$. The range was chosen to be wider than the dust grain size range ($3 \mu\text{m}$ – 3 mm , see Table 2) in order to account for micro-pores at the low-end, and to enable the flow of a few mm-size grains

Table 3: Initial composition of 9P/Tempel1 models

Constituent mass fraction	Working model: Trapped gas No mantle	Trapped gas Dust mantle	Ice mixture No mantle	Ice mixture Dust mantle
X_a	0.5	0.5	0	0
X_c	0	0	0.45	0.45
X_d	0.5	0.5	0.5	0.5
X_{CO}	0.05	0.05	0.025	0.025
X_{CO_2}	0.0125	0.0125	0.00625	0.00625
X_{HCN}	0.0035	0.0125	0.00625	0.00625
X_{NH_3}	0.0125	0.0125	0.00625	0.00625
$X_{C_2H_2}$	0.0012	0.0125	0.00625	0.00625

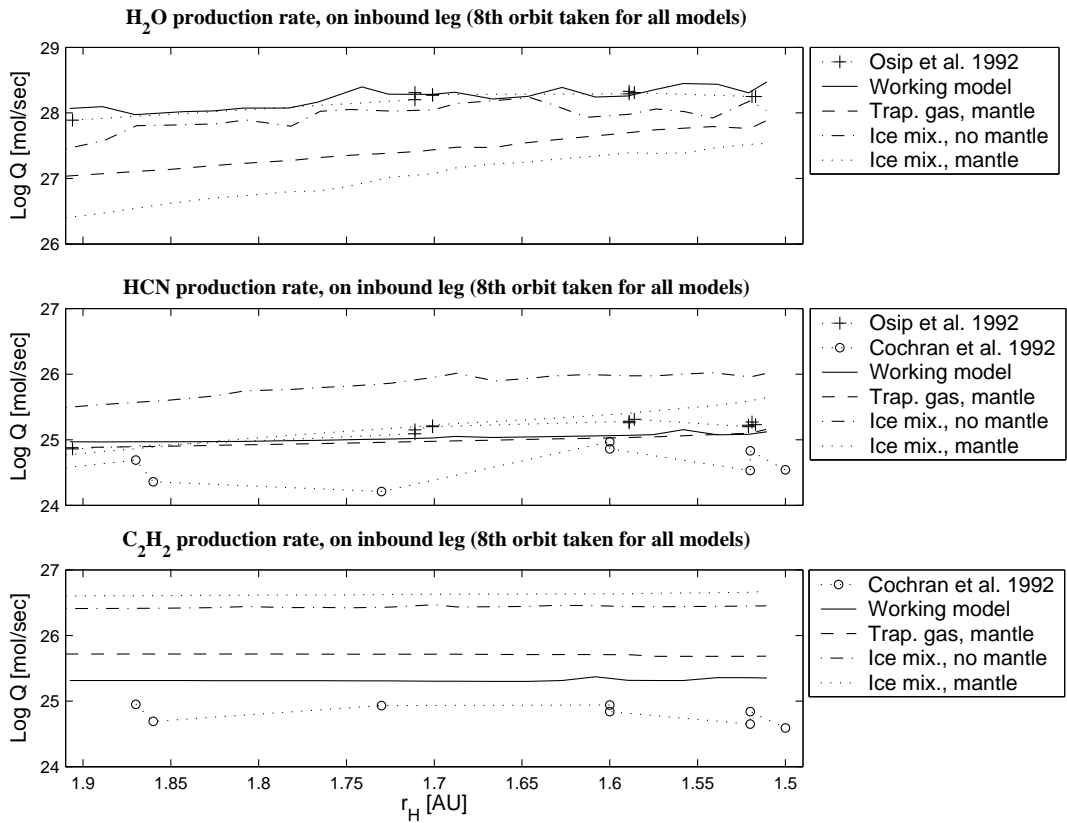


Fig. 3.— Comparison of observation and model run results for 4 generic models, as described in the paper. Observed production rate of OH, as the product of H_2O , CN, as the product of HCN, and C_2 , as the product of C_2H_2 , were taken from the references.

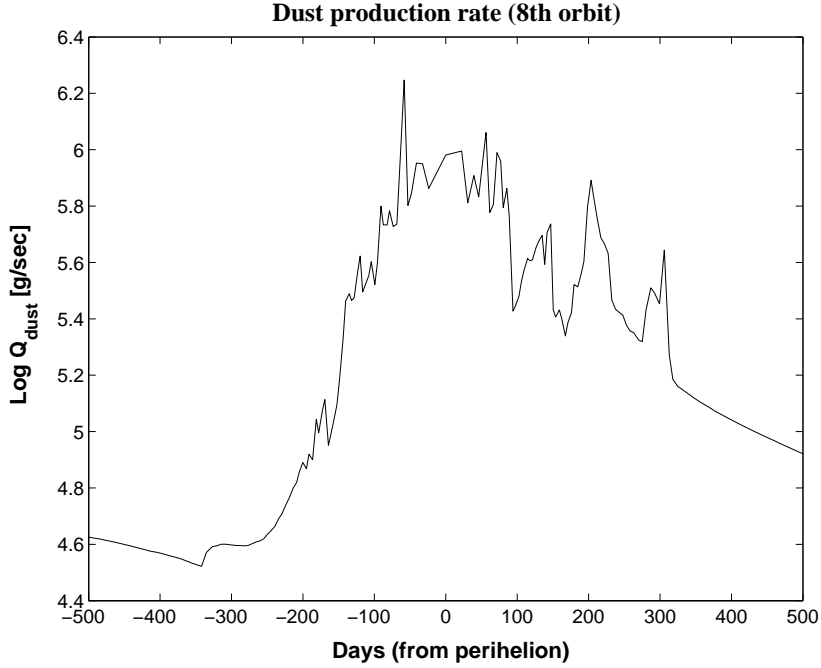


Fig. 4.— Dust production rate pre- and post-perihelion for the baseline model.

requiring somewhat larger pores at the high-end. A steeper power law was chosen for pore sizes than indicated by grain observations, because dust grains are also lifted off the surface, where pore size does not constitute an impediment, and hence the relative proportion of larger grains coming from the surface should be larger than for those originating from the interior.

Assuming the spin axis to be perpendicular to the orbital plane and starting with a uniform low temperature, we followed the evolution of the working model for several orbits. The thermal and compositional evolution is illustrated in Fig.5, for the subsolar point on the equator and for a point near the pole. These represent extreme cases — maximum and minimum — with respect to absorption of solar radiation, and hence activity, of a spinning nucleus in the orbit of 9P/Tempel 1, among *all* possible inclinations of the spin axis. We recall that the model nucleus is spherical, whereas in reality the nucleus is found to be highly elongated, with semi-axes $a \approx 7.2$ km, $b \approx c \approx 2.2$ km (Belton et al. 2005). Thus the "collecting area" of the nucleus may vary, according to inclination, between $\sim 15 - 50$ km², compared to 34 km² of the model. This would place an error bar of up to a factor of 2 on the results regarding production rates, since most of the solar heat is spent in sublimation of volatiles. The shape itself should be of lesser importance, since the affected layer, as we shall see, is much smaller than the radius.

The outstanding feature emerging from this calculation is the complicated stratification pattern as a function of depth, where layers enriched in various volatiles alternate. Moreover, several layers enriched in the same volatile may appear at different depths. The effect is illustrated by the mass fraction of amorphous ice shown in the right panels of Fig.5. We recall that the model’s composition includes 5 volatile species trapped in amorphous water ice. These volatiles cover a wide range of sublimation temperatures (see Prialnik et al. 2005). As the surface of the nucleus is heated and the heat wave propagates inward, the amorphous ice crystallizes and the trapped gas is released. The gas pressure in the pores peaks at the crystallization front. As a result, gas flows in part outward and escapes, and in part, inward into colder regions. Eventually, each species reaches a sufficiently cold region for it to recondense. Since recondensation releases heat, it affects the composition of its surroundings and thus a complicated pattern results, of alternating ices mixed with the amorphous water ice. When another heat wave reaches these regions, on a subsequent perihelion passage, the heat is absorbed in sublimation of the recondensed volatiles rather than in crystallization of amorphous ice. This is how alternating layers of crystalline and amorphous ice arise, rather than a single boundary between a crystalline exterior and an amorphous interior. Finally, the *steps* that appear in the outer crystalline/amorphous ice boundary are due to erosion of the nucleus, which brings this boundary closer to the surface.

The stratified layer extends from a depth of about 10 m below the surface and down to a few hundred meters. Since 10 m is roughly the orbital skin depth for 9P/Tempel 1, this structure should cause activity variations on the orbital time scale. This means that activity may differ from orbit to orbit and occasional spurious outbursts may arise, when the heat wave propagating down from the surface reaches a region enriched in ice of some volatile species. Such outbursts of gas should be accompanied by ejection of dust. Indeed, this variable behavior is exhibited in Fig.6, where we note an outburst of gas (CO and CO₂) and dust following several "quiet" regular orbits. By contrast, water production, whose main source is sublimation from the surface, follows a much more regular pattern.

The evolution of local noon temperature profiles is shown in the left panels of Fig.5. It indicates that a steady state is reached in each case after a few revolutions at about the same depth, both near the pole and at the equator. This depth corresponds to the orbital skin depth $[2Ka^{3/2}/(\sqrt{GM_{\odot}}\rho c)]^{1/2} \approx 10$ m. We note, however, that the maximum temperatures at the two locations differ by about 40 K; accordingly, the skin depth, which is roughly inversely proportional to temperature, is slightly larger near the pole. Without the correction factor to the SVR, internal temperatures are somewhat higher in the outer layers since less heat is absorbed in ice sublimation.

We now wish to draw attention to the effect of the corrected SVR on the results.

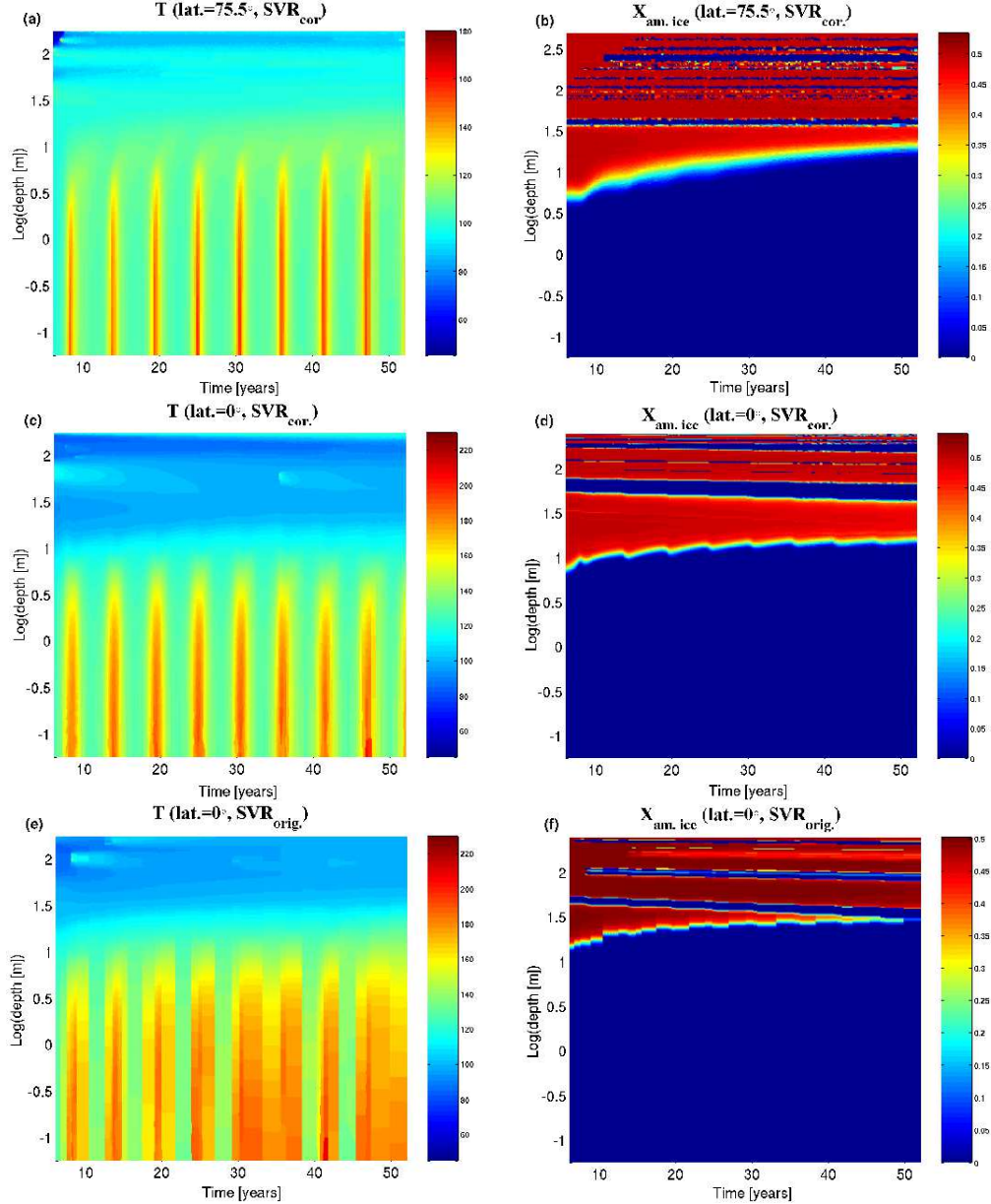


Fig. 5.— Evolution of the comet nucleus working model through repeated revolutions. The temperature and amorphous ice abundance are shown as a function of time and depth: (a) and (b) — near-pole latitude, with the corrected SVR term; (c) and (d) — equator, with the corrected SVR term; (e) and (f) — equator, with the original SVR term. The depth scale is logarithmic, from the surface to the interior.

Temperature profiles at the equator are compared in Fig.5 in the two lower left panels, and the evolution of crystallization in the two lower right panels. The correction factor increases the internal pore surface and enhances sublimation from the pore walls. This hinders the heat wave from penetrating deeper and internal temperatures are thus lower. As a result, the depth of amorphous ice is shallower, as illustrated in Fig.5. At higher latitudes, due to the diminished insolation, it is still shallower.

Production rates obtained for long-term evolution with and without the SVR correction are compared in Fig.6. As expected, surface properties, such as temperature and H₂O production rate, are not affected. The production rates of gases released in the interior, either escape from crystallizing ice or by sublimation of recondensed ice, are affected to a larger extent, but preserve the same pattern of behavior. This is not surprising, since the driving energy source is the same. We note that the complex stratified structure of the outer layer of the nucleus gives rise to occasional outbursts. Clearly, the orbital evolution of production rates differs considerably among different volatiles. This means that observed volatile abundances do not reflect nucleus abundances (cf. Huebner and Benkhoff 1999, Prialnik et al. 2005).

6. Simulation of a deep impact

The aim of the *Deep Impact* mission is the collision of the impactor spacecraft with the nucleus, in order to create a crater. This will enable the flyby spacecraft to perform observations and measurements of the impact itself, the ejected material and the interior composition, as revealed by the exposed crater.

The thermal effect of the impact is simulated by assuming an additional energy influx for an infinitesimal period of time. The known input parameters for the impact simulation are the total (kinetic) energy of the projectile E_{tot} , the estimated area A , that will be affected by the impact — which is needed in order to obtain an energy flux — and the heliocentric distance (preperihelion) where the impact is expected to take place, d_0 . The total energy absorbed per unit area is $E_A = E_{\text{tot}}/A$. We note that the relevant parameter is E_A , hence the calculation is not sensitive to the total impact energy or the area, separately.

Since numerical calculations do not allow singularities, we assume the energy deposition rate to be in the form of a narrow time-dependent Gaussian (rather than a delta function), *centered* at the time of the impact, with a width corresponding to the timescale for the formation of the crater,

$$F(t) = F_0 e^{-\pi[(t-t_0)/\tau]^2}. \quad (25)$$

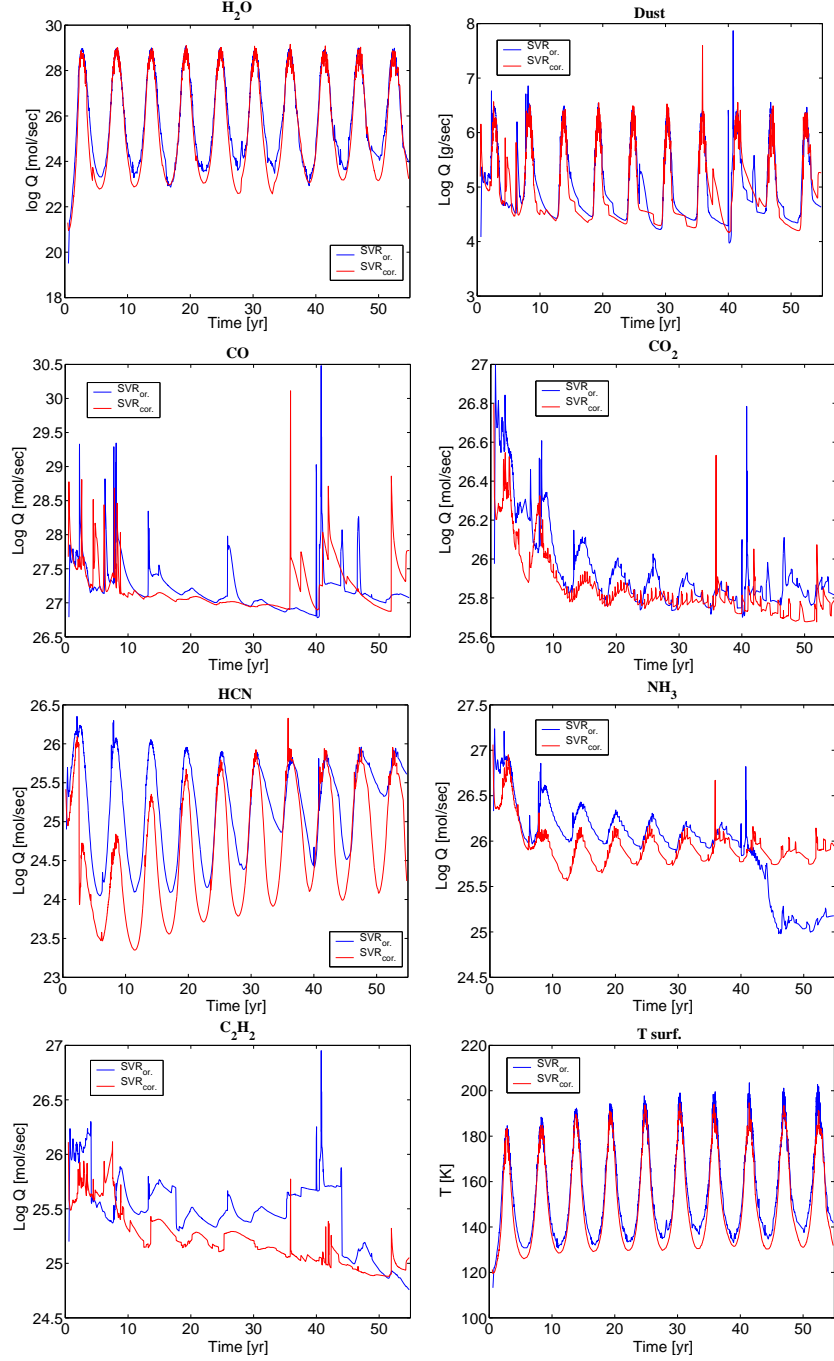


Fig. 6.— Comparison of original SVR (blue) and corrected SVR (red), for 10 orbits of the working model: results are shown for the surface temperature at the subsolar point as well as production rates for all volatiles and dust.

Table 4: Impact simulation properties

Parameter	Symbol	Value	Units
Total energy	E_{tot}	1.9×10^{10}	J
Crater area	A	1000	m^2
Crater depth	ΔL	30	m
Heliocentric distance	d_0	2	AU
Revolutions before impact	n	7	
Timescale	τ	180	s
Peak energy flux	F_0	10^5	$\text{J m}^{-2} \text{ s}^{-1}$

Here τ is a free numerical parameter that may be interpreted as the impact timescale. Normalizing the deposition rate,

$$\int_{-\infty}^{\infty} F(t)dt = E_A \quad (26)$$

we obtain $F_0 = E_A/\tau$. Thus, the amplitude of the energy deposition rate is related to the physical parameters of the impact. The parameter values used are listed in Table 4. The resulting peak energy flux is about 300 times higher than the solar energy flux at that distance at the subsolar point. At a distance of 1.5 AU, the current impact distance, the contrast would be reduced by a factor of ~ 0.6 , but this change should not be significant. The time of impact t_0 is calculated by

$$t_0 = \sqrt{a^3/GM_{\odot}}(2\pi n - \pi - \vartheta_0 + e \sin \vartheta_o) \quad (27)$$

$$\vartheta_0 = \cos^{-1}[(1 - d_0/a)/e], \quad (28)$$

where n is the number of orbital revolutions calculated prior to the impact.

At the onset of the impact — defined to occur at a time $t_0 - \nu\tau$, where $\nu > 1$, so that $F(t \pm \nu\tau) \ll F_0$ — we remove from the model nucleus a layer of thickness $\Delta L \approx 30$ m, to simulate the crater that is expected to form. Thus the thermal energy is deposited below the original nucleus surface, where the composition had been either preserved, or altered by earlier evolution to a different extent. We should bear in mind that the thermal effect of the impact is maximized, since it is assumed that the entire kinetic energy is turned into heat and the heat is all deposited at a depth corresponding to the bottom of the impact crater.

Two impact calculations were carried out for two different locations on the nucleus surface: one at the equator, and another near the pole. The purpose was to find out to what extent is the point of impact expected to affect the outcome. The comparison of the

two locations is presented in Fig.7, and shows that, to within a fraction of a magnitude, the production rates of the major constituents (H_2O , dust, CO and CO_2) are indistinguishable at the moment of impact. However, since the flyby spacecraft is supposed to conduct the observation for a period of ~ 15 minutes after the impact, the emission of dust, CO and CO_2 may vary by ~ 2 orders of magnitude during this time.

The low production rates before impact are an artifact of our simulation: when we remove an outer layer of several tens of meters, we expose cold material. Since the energy is supplied slowly at first, production rates drop. The total amount of dust ejected upon impact amounts to $\sim 1.7 \times 10^5$ tons at the near-pole location, and $\sim 2.2 \times 10^5$ tons near the equator. Compared with the dust production rate over the entire comet at perihelion, these amounts are equivalent to the total dust output of 2 days and 2.6 days, respectively, at perihelion.

We note that the CO and CO_2 ejection rates are not smooth: they show two spikes and a somewhat later peak (see Fig.7). This is due to the layered structure of the nucleus described in Section 5. The fact that the behavior pattern of these volatiles is reflected in the rate of dust ejection indicates that a significant fraction of the dust originates in layers beneath the surface. Small dust grains are thus dragged by volatiles through the pores. This effect is less marked near the pole, where the subsurface layers have been processed to a far lesser extent during evolution prior to the impact.

An interesting result of the long-term evolution, is that even though the thermal energy influx due to the impact is confined in both time (by the Gaussian function) and space (by the depth of penetration), the effect lingers and shows deviations in production rates - as compared with the undisturbed model - long after the event. However, this effect cannot be used to characterize a comet that has undergone an "impact", because the evolution pattern is similar to that of a comet model that was not disturbed. The difference is in the detailed variation of production rates with heliocentric distance, but these details depend to a similar extent on model parameters and assumptions.

7. Conclusions

We have followed the evolution of a rotating nucleus model in the orbit of comet 9P/Tempel 1 for several orbits, until a quasi-steady-state was attained, and then we have simulated an impact, similar in energy to the projectile of the *Deep Impact* mission, focusing on the thermal outcome. A similar effect may be expected of a random collision with a large meteor. Provided that such a collision will create a deep crater and expose layers a few tens of meters

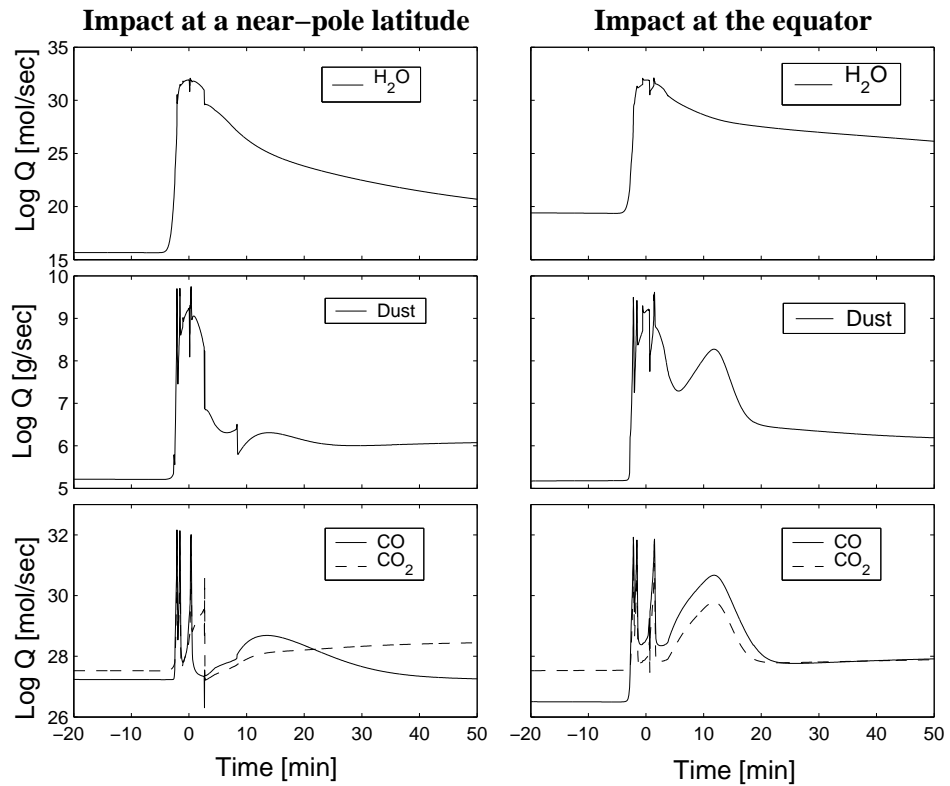


Fig. 7.— Comparison between the two extreme of impact latitudes: near-pole (75.5°) and equator (0°). The dominant volatiles, H_2O , CO and CO_2 , and the dust component, are presented at high temporal resolution, around the peak of the impact. Note that the general shape of production rates is similar at both impact sites.

deep, an outburst of gas and dust ejection is expected to result. This is due to the fact that at such depths, ices of volatile species should be present, as well as amorphous water ice, which may crystallize by absorbing the impact heat and release more volatiles. Our main results regarding the outcome of the impact are as follows.

- The increase in production rate of volatiles and dust is of several orders of magnitude, and thus readily observable. The total dust output, for example, is equivalent to the output of about two days at perihelion. We should bear in mind, however, that these results provide an upper limit, since it is assumed that the entire energy is spent in thermal effects.
- An important conclusion of these calculations is that the place on the nucleus where the impact occurs is not as significant as one might expect. The total dust output, for example, differs by only a factor of ~ 1.3 .
- Variability in the comet's activity may be detected even on the short time scale of the impact, as the heat wave propagates into a layer of stratified composition, where amorphous water ice may crystallize and ices of various volatile species may sublimate.
- Subsequent long-term thermal evolution is also affected to some extent, but not in a way that would be recognized by observations as an aftermath of an impact (or collision). The variation of volatile production rates with time (or heliocentric distance) will retain a general uneven pattern, but whether this pattern differs from that of an undisturbed comet may be difficult to establish.

It should be borne in mind that these predictions are based on a simplified model of a real comet.

We would like to thank Björn Davidsson for a careful reading of the manuscript and many helpful comments. Support for this work was provided, in part, by Israel Science Foundation grant No.942/04 and in part, through University of Maryland and University of Hawaii subcontract Z667702, which was awarded under prime contract NASW-00004 from NASA.

References

A'Hearn, M. F., Belton, M. J. S., Delamere, A., Blume, W. H. (2005) Deep Impact: A large-scale active experiment on a cometary nucleus. *Space Science Reviews*, in press.

Belton, M. J. S., A'Hearn, M. F. (1999) Deep sub-surface exploration of cometary nuclei. *Advances in Space Research* 24, 1175–1183.

Belton, M. J. S., Meech, K. J., A'Hearn, M. F., Groussin, O., McFadden, L., Lisse, C., Fernández, Y. R., Pittichová, J., Hsieh, H., Kissel, J., Klaasen, K., Lamy, P. L., Prialnik, D., Sunshine, J., Thomas, P., Toth, I. (2005) Deep Impact: Working properties for the target nucleus - Comet 9P/Tempel 1. *Space Science Reviews*, in press.

Cochran, A. L., Barker, E. S., Ramseyer, T. F., Storrs, A. D. (1992) The McDonald Observatory Faint Comet Survey - gas production in 17 comets. *Icarus* 98, 151–162.

Cohen, M., Prialnik, D., Podolak, M. (2003) A quasi-3D model for the evolution of shape and temperature distribution of comet nuclei - application to comet 46P/Wirtanen. *New Astronomy* 8, 179–189.

Crifo, J. F., Rodionov, A. V. (1997) The dependence of the circumnuclear coma structure on the properties of the nucleus. *Icarus* 129, 72–93.

Davidsson, B. J. R., Skorov, Y. V. (2002) On the light-absorbing surface layer of cometary nuclei. I. Radiative transfer. *Icarus* 156, 223–248.

Davidsson, B. J. R., Skorov, Y. V. (2002) On the light-absorbing surface layer of cometary nuclei. II. Thermal modeling. *Icarus* 159, 239–258.

Davidsson, B. J. R., Skorov, Y. V. (2004) A practical tool for simulating the presence of gas comae in thermophysical modeling of cometary nuclei. *Icarus* 168, 163–185.

Fanale, F. P., Salvail, J. R. (1984) An idealized short-period comet model - Surface insolation, H₂O flux, dust flux, and mantle evolution. *Icarus* 60, 476–511.

Farnham, T. L. (1996). PhD Thesis, University of Hawaii.

Fernández, Y. R., Meech, K. J., Lisse, C. M., A'Hearn, M. F., Pittichová, J., Belton, M. J. S. (2003) The nucleus of *Deep Impact* target Comet 9P/Tempel 1. *Icarus* 164, 481–491.

Finson, M. L., and R. F. Probstein (1968). A theory of dust comets. *Ap. J.* 154, 327.

Fulle, M., Mikuz, H., Bosio, S. (1997) Dust environment of Comet Hyakutake 1996B2. *Astronomy and Astrophysics* 324, 1197–1205.

Gombosi, T. I. (1994) Gaskinetic theory, Cambridge: Cambridge University Press.

Harker, D. E., Wooden, D. H., Woodward, C. E., Lisse, C. M. (2002) Grain properties of Comet C/1995 O1 (Hale-Bopp). *Astrophysical Journal* 580, 579–597.

Housen, K. R. (2002) Does gravity scaling apply to impacts on porous asteroids? *Lunar and Planetary Science XXXIII*, 1969.

Huebner, W. F., Benkhoff, J. (1999) On the relationship of chemical abundances in the nucleus to those in the coma. *Earth, Moon and Planets* 77, 217–222.

Jockers, K. (1999) Observations of scattered light from cometary dust and their interpretation. *Earth, Moon and Planets* 79, 221–245.

Lamy P. L., Toth, I., A'Hearn, M. F., Weaver, H. A., Weissman, P. R. (2001) Hubble Space Telescope observations of the nucleus of 9P/Tempel 1. *Icarus* 154, 337–344.

Landolt, A. U. (1992) UBVR photometric standards stars in the magnitude range $11.5 < V < 16.0$ around the celestial equator. *Astronomical Journal* 104, 340–370.

Marsden, B. G. (1963) On the orbit of some long lost comets. *Astronomical Journal* 68, 795–801.

Meech, K. J., A'Hearn, M. F., McFadden, L., Belton, M. J. S., Delamere, A., Kissel, J., Klassen, K., Yeomans, D., Melosh, J., Schultz, P., Sunshine, J., Veverka, J. (2000) Deep Impact - Exploring the interior of a comet, in *A new era in Bioastronomy*, ASP Conference Series 213, G. A. Lemarchand, K. J. Meech, eds. Astronomical Society of the pacific, 235–242.

Meech, K. J. (2002) The Deep Impact mission and the AAVSO. *Journal of the American Association of Variable Star Observers* 31, 27–33.

Meech, K. J., A'Hearn, M. F., Fernández, Y. R., Lisse, C. M., Weaver, H. A., Biver, N., Woodney, L. M. (2005) The Deep Impact Earth-Based Campaign. *Space Science Reviews*, in press.

Mekler, Y., Prialnik, D., Podolak, M. (1990) Evaporation from a porous cometary nucleus. *Astrophysical Journal* 356, 682–686.

Nolan, M. C., Asphaug, E., Melosh, H. J., Greenberg, R. (1996) Impact craters on asteroids: does gravity or strength control their size? *Icarus* 124, 359–371.

Osip, D. J., Schleicher, D. G., Millis, R. L. (1992) Comets - Groundbased observations of spacecraft mission candidates. *Icarus* 98, 115–124.

Podolak, M., Prialnik, D. (1996) Models of the structure and evolution of comet P/Wirtanen. *Planetary and Space Science* 44, 655–664.

Prialnik, D. (1992) Crystallization, sublimation, and gas release in the interior of a porous comet nucleus. *Astrophysical Journal* 388, 196–202.

Prialnik D., Benkhoff, J., Podolak, M. (2005) Modeling the Structure and Activity of Comet Nuclei, in *Comets II*, M. Festou, H. U. Keller, H. A. Weaver, eds. University of Arizona Press, 359–387.

Schmitt, B., Espinasse, S., Grim, R. J. A., Greenberg, J. M., Klinger, J. (1989) Laboratory studies of cometary ice analogues. *ESA SP 302 (Physics and Mechanics of Cometary Materials)*, 65–69.

Schultz, P. H., Anderson, J. L. B., Heineck, J. T. (2002) Impact crater size and evolution: expectations for Deep Impact. *Lunar and Planetary Science XXXIII*, 1875.

Schultz, P. H., Anderson, J. L. B. (2005) Alternative cratering scenarios for the Deep Impact collision. *Lunar and Planetary Science XXXVI*, 1926.

Wünnemann, K., Collins, G. S., Melosh, H. J. (2005) Numerical modeling of the Deep Impact mission experiment. *Lunar and Planetary Science XXXVI*, 1837.